

Long-range backscatter from the Mid-Atlantic Ridge

Nicholas C. Makris and Jonathan M. Berkson
Naval Research Laboratory, Washington, DC 20375

(Received 2 June 1993; accepted for publication 10 October 1993)

Acoustic backscatter returns measured with a vertical source and horizontal receiving array are beamformed and charted to respective scattering sites on the western flank of the Mid-Atlantic Ridge (MAR). Well-defined patterns of high-level backscatter resembling bottom morphology occur within the direct path and at convergence zone ranges. Measured backscatter is compared with modeled two-way transmission loss using the wide-angle parabolic equation (PE) and high-resolution supporting bathymetry. The level of backscatter is found to be strongly dependent upon two-way transmission loss (TL). Specifically, TL selects prominent bathymetric features from which high backscatter is returned, with backscatter maxima corresponding to TL minima. Scattering strength estimated for the wide area surveyed shows low variance and relatively minimal spatial variation. Apparently, distinct scattering contributions are so well mixed in long-range backscatter, that dominant variations are generally due to propagation. These results indicate that it is possible to forecast the range and azimuth of prominent MAR backscatter returns simply by propagation modeling if high-resolution bathymetry is available. They also have led to the development of a new technique for ambiguity removal in reverberation data measured with a horizontal line array. The method takes advantage of environmental asymmetry provided by TL in highly range-dependent environments and does not require multiple measurements as do other existing methods.

PACS numbers: 43.30.Bp, 43.30.Gv, 43.30.Vh

INTRODUCTION

In July and August of 1991 acoustic reverberation data were acquired above the western flank of the Mid-Atlantic Ridge (MAR). A single research vessel towed a vertical source and horizontal receiving array to obtain quasimonostatic measurements of ocean-bottom reverberation at low frequency. The three-week experiment covered a large area and employed a broad range of waveforms as well as impulsive charges. Data were recorded long enough to address a variety of direct-path and long-range reverberation issues. Since sea states were generally below Beaufort Force 1, interference from surface reverberation was negligible and data quality was high. Referred to as the Acoustic Reconnaissance Cruise (ARC), the experiment is part of an on going Special Research Program (SRP) on bottom reverberation sponsored by the Office of Naval Research.^{1,2} In August of 1992, a supporting database of high-resolution bathymetry³ was obtained for the region previously surveyed by the ARC.

Our goal is to understand the relationship between backscatter returning from multiple convergence zone (CZ) ranges and complex geomorphology in the deep ocean. Previous investigators have found a correspondence between long-range backscatter measured via towed array and gross bathymetry.⁴⁻⁸ In an analysis of Tyrrhenian sea data, Nghiem-Phu and Tappert have shown that range-dependent modeling of two-way transmission loss (TL) with the parabolic equation (PE) can determine the general characteristics of backscatter without detailed information about individual scattering sites.⁹ However, this as well as other past studies have focused upon environments where isolated large-scale scattering features, such as sea-

mounts or continental margins, penetrate or curtail sound channels which are otherwise generally free from bottom interaction. In these situations, gross bathymetric surveys are sufficient for a first-order modeling of TL.

The ARC stands apart because it was carried out in the previously uninvestigated MAR where rugged bathymetry projects small-scale features into the deep sound channel. As a result, bottom limitation of deep-sound-channel propagation is extensive and highly variable for sources at depths used in typical sonar systems. Reverberation in such complex environments has not been thoroughly investigated in the past, and is interesting because of the numerous returns found over range and azimuth which generally serve as false targets in active sonar measurements. Only with the recent availability of high-resolution bathymetry, collected in support of SRP acoustic data, has it become possible to study the relationship between reverberation and small-scale geomorphology in the MAR. Such analysis is not only useful for sonar design in highly reverberant environments, but may also provide a practical method for remote survey of complex bathymetry. In this paper, we show that long-range backscatter is highly correlated with small-scale geomorphology and that this correlation can be largely explained by TL modeling with high-resolution bathymetry.

To describe our method of charting backscatter we find it convenient to introduce the following definitions. We define an "observation" as a single active insonification and subsequent towed-array measurement of reverberation where the array position and orientation can be considered constant. We define a "reverberation map" as the magnitude of acoustic returns from a single observation charted

Report Documentation Page				Form Approved OMB No. 0704-0188	
Public reporting burden for the collection of information is estimated to average 1 hour per response, including the time for reviewing instructions, searching existing data sources, gathering and maintaining the data needed, and completing and reviewing the collection of information. Send comments regarding this burden estimate or any other aspect of this collection of information, including suggestions for reducing this burden, to Washington Headquarters Services, Directorate for Information Operations and Reports, 1215 Jefferson Davis Highway, Suite 1204, Arlington VA 22202-4302. Respondents should be aware that notwithstanding any other provision of law, no person shall be subject to a penalty for failing to comply with a collection of information if it does not display a currently valid OMB control number.					
1. REPORT DATE APR 1994		2. REPORT TYPE		3. DATES COVERED 00-00-1994 to 00-00-1994	
4. TITLE AND SUBTITLE Long-range Backscatter from the Mid-Atlantic Ridge				5a. CONTRACT NUMBER	
				5b. GRANT NUMBER	
				5c. PROGRAM ELEMENT NUMBER	
6. AUTHOR(S)				5d. PROJECT NUMBER	
				5e. TASK NUMBER	
				5f. WORK UNIT NUMBER	
7. PERFORMING ORGANIZATION NAME(S) AND ADDRESS(ES) Naval Research Laboratory, 4555 Overlook Ave SW, Washington, DC, 20375				8. PERFORMING ORGANIZATION REPORT NUMBER	
9. SPONSORING/MONITORING AGENCY NAME(S) AND ADDRESS(ES)				10. SPONSOR/MONITOR'S ACRONYM(S)	
				11. SPONSOR/MONITOR'S REPORT NUMBER(S)	
12. DISTRIBUTION/AVAILABILITY STATEMENT Approved for public release; distribution unlimited					
13. SUPPLEMENTARY NOTES					
14. ABSTRACT					
15. SUBJECT TERMS					
16. SECURITY CLASSIFICATION OF:			17. LIMITATION OF ABSTRACT Same as Report (SAR)	18. NUMBER OF PAGES 17	19a. NAME OF RESPONSIBLE PERSON
a. REPORT unclassified	b. ABSTRACT unclassified	c. THIS PAGE unclassified			

to the horizontal location of respective scattering sites. To generate reverberation maps from ARC data, we first estimate the range and azimuth of scattering sites by two-way travel time analysis and beamforming. Since beamformed line-array data have an inherent right-left ambiguity about the array's axis it is especially challenging to identify true from virtual scattering sites in the MAR where ambiguous returns are broadly distributed in range and azimuth.

The ARC tow-ship tracks were designed to provide a general survey of backscatter in the vicinity of the western MAR. They are not optimal for the existing methods of ambiguity removal which rely upon multiple adjacent observations at different array heading.^{10,11} Therefore, we introduce a method based upon two-way TL modeling with the wide-angle PE,¹² and use this in our subsequent data analysis. This method has a strong physical foundation which takes advantage of naturally occurring asymmetries in the MAR environment by incorporating the high-resolution bathymetry database. Unlike other ambiguity resolution methods, it does not require multiple data observations. Further, it can be applied objectively to the entire data set. This is in contrast to ambiguity resolution by comparison with bathymetry which is extremely subjective, and biased toward discrete or well-defined returns.

Once ambiguity is resolved, backscatter levels are unambiguously projected onto bathymetry for comparison. We find that prominent returns occur at $n + \frac{1}{2}$ CZ ranges and are well correlated with ridges which have extended scarps facing the observation, where $n=0, 1$ for the present survey. However, resolution is too poor to determine whether this correlation is solely due to a propagation effect which insonifies the backfacing scarps of prominent ridges, or whether it is also due to the orientation and geomorphology of scatterers within the ridges. Finally, we combine modeled TL with unambiguous backscatter level to estimate scattering strength over the wide-area surveyed. Our technique introduces two advances over more traditional scattering strength estimation: (a) TL is computed using a full-field propagation model rather than a raytrace; (b) the area term of the sonar equation is incorporated by a spatial convolution rather than a constant scale factor.

I. A HIGHLY BOTTOM-LIMITED ENVIRONMENT

A. Observation geometry

We analyze only a small fraction of the total ARC reverberation data set for the present study, focusing on data measured central to the bathymetry database. We classify observations by track, or run number (R), and emission sequence, or epoch number (E). The observations for the present study are then labeled R7E10 and R7E15 in Fig. 1 where track information is superposed on an image generated from the high-resolution bathymetry, sampled at 200-m intervals. For example, track 7 runs from north to south.

B. Long-range propagation corridors

Some general characteristics of the acoustic field incident upon the ocean bottom can be readily deduced from source, sound speed, and bathymetric information. The source/receiver deployment geometry is indicated in Fig. 2, along with miscellaneous operational characteristics of the arrays. Due to negligible horizontal variation,¹³ a single representative sound-speed profile, shown in Fig. 3, can be used to describe the water column. While the density, sound speed, and attenuation of the bottom vary in both the horizontal and vertical, information about these parameters is limited. However, we do know that sediment of varying thickness and relatively homogeneous acoustic impedance covers a majority of the survey area.¹⁴ Therefore, we assume the bottom is comprised of sediment with uniform density 1.5 g/cm³, sound speed 1700 m/s, and attenuation 0.5 dB/λ for all range-dependent acoustic modeling done in this paper.

An example of deep sound channel propagation characteristic to the ARC is shown in Fig. 4 for a range-depth cross section of the ocean. An idealized flat bottom at 5-km depth is used to demonstrate the CZ structure of the source beam when undisturbed by bottom interaction, which is a rare situation for our survey. Propagation modeling is done with the wide-angle PE for the environmental parameters discussed above. The source array is accurately modeled by ten omnidirectional monopoles at depths corresponding to those of the actual projectors. The model source elements are horizontally steered and operate at 270 Hz. The combined TL is normalized so that a single source level may be applied to obtain sound-pressure level at any point in the field.

The source beam contains the highest amplitude sound waves by orders of magnitude. The beam has a complex structure due to interference caused by the source's proximity to the pressure release surface; the numerous side-lobes of the untapered source array; and the refractive properties of the water column which lead to deep-sound-channel propagation. It has a first deep vertex approximately 33 km from the source, which defines the $\frac{1}{2}$ CZ range, the region within which is referred to as the direct-path area. Here beam vertex occurs between roughly 3900- and 4500-m depth. For practical considerations then, the beam will propagate undisturbed in the water column for bathymetry exceeding 4500 m, will be partially blocked or reflected for bathymetry between 4500 and 3900 m, and will be totally blocked or reflected for bathymetry shallower than 3900 m.

To consolidate this information, we employ the following terminology. "Conjugate depth" refers to the depth below the minimum sound speed where the sound speed returns to the value at the source center. Conjugate depth occurs at roughly 3900 m for the ARC. (By Snell's law, horizontal rays emanating from the source will vertex at conjugate depth.) The term "excess depth" refers to the difference between bathymetric depth and conjugate depth. And, "positive excess depth" occurs for bathymetric depths exceeding the conjugate depth.

To give an overview of the anticipated blockages in

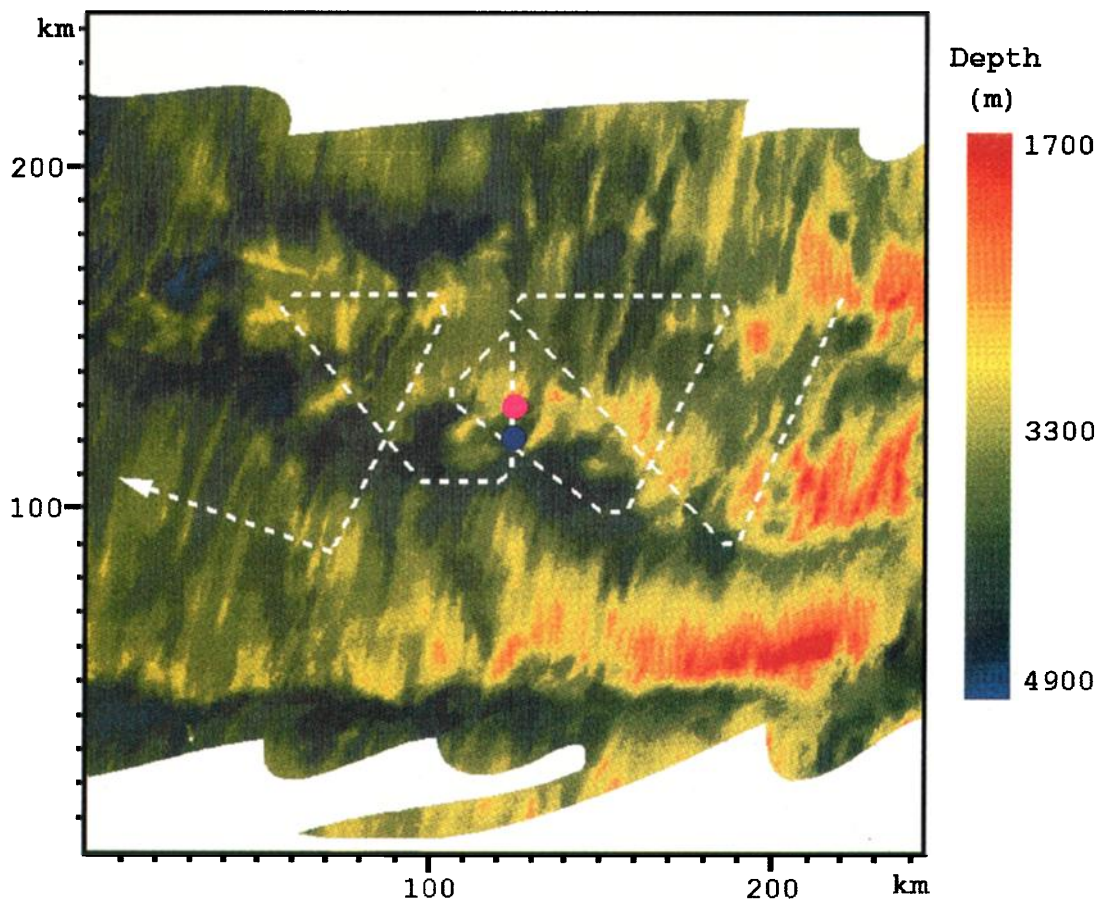


FIG. 1. Hydrosweep bathymetry from SRP geophysical survey of 1992 gridded at 200-m intervals.³ The dotted white line indicates the tracks, or straight line runs, of the research vessel. The colored dots indicate the position of monostatic backscatter observations relevant to this investigation. The observations are labeled R7E10 and R7E15 for the northern and southern observations, respectively. The irregular border within the figure indicates the limit of hydrosweep coverage.

multiple CZ propagation, we have plotted the bathymetry where positive excess depth is available, in Fig. 5, and note that this comprises less than 50% of the area surveyed. Two concentric circles centered about observation R7E15, closest to the track crossing, are superposed on the

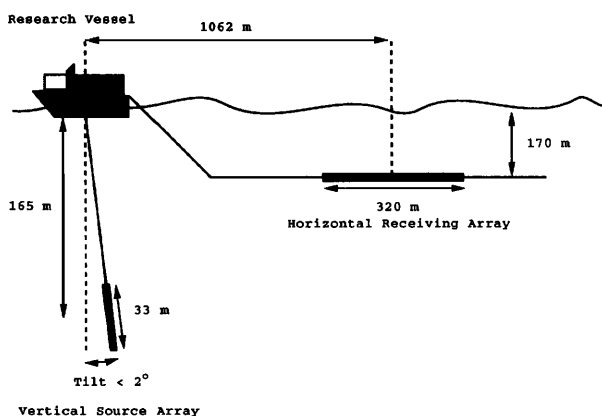


FIG. 2. A sketch of the research vessel towing the vertical source and horizontal receiving arrays. Array depths and orientation change with ship's speed. Conditions shown are for a typical tow speed of 3.5 kn. The element spacing is 3.66 m for the vertical array and 2.50 m for the horizontal array.

bathymetry. These indicate the $\frac{1}{2}$ and $1\frac{1}{2}$ CZ radii as if there was no bottom interaction. In reality, however, bottom interaction is extensive. The $\frac{1}{2}$ CZ circle's intersection with positive excess depth is limited to relatively narrow azimuths to the southwest and southeast of the observation. Only along these restricted azimuths do we anticipate multiple CZ propagation to be possible. At all other azimuths, bottom interaction within the direct-path area will cause the source beam to be attenuated and redistribution in vertical angle, resulting in much weaker long-range insonification. Therefore, only a sparse azimuthal distribution of scattering sites at $1\frac{1}{2}$ CZ range will be insonified by waterborne paths. This is significant because the strongest backscatter is expected to return from sites where waterborne paths are available.

To demonstrate the environmental symmetry breaking potential available in range-dependent propagation modeling, we have strategically selected radials for PE runs. The radials extend from observation position R7E15 and are comprised of ambiguous pairs (α, α') and (β, β') about the array axis. Radials α and β , respectively, intersect the southwestern and southeastern azimuths where positive excess depth is available at $\frac{1}{2}$ CZ. This is displayed in Fig. 5. Bathymetry from the high-resolution database is extracted along each radial to supply range dependence in each run.

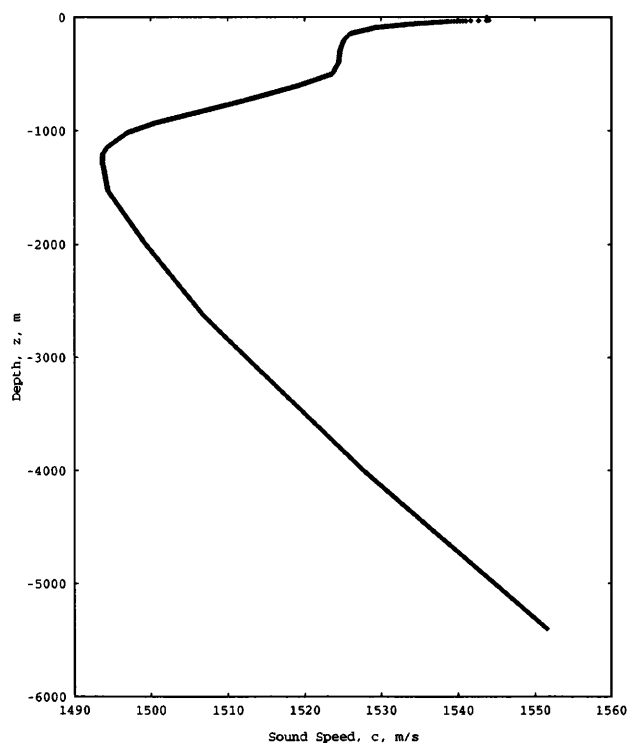


FIG. 3. A sound-speed profile typical of those measured via XBT during the ARC. The cast was taken approximately 18-km south of the central observation R7E15 on run 7. Archival data used below the 2000-m depth.

To be consistent with ARC steering and source frequency for the data analyzed in this paper, the modeled source elements are steered to a depression angle 6° from horizontal and operate at 270 Hz. Range-depth cross sections of the propagation along each radial are shown in Fig. 6. First, consider propagation along radial α where a waterborne path is available to a bottom site at roughly $1\frac{1}{2}$ CZ. Here TL is substantially lower than at the ambiguous $1\frac{1}{2}$ CZ site along radial α' . This is because along α' , the source beam is terminated within the direct-path area. Therefore, backscatter of much higher amplitude is expected from the $1\frac{1}{2}$ CZ bottom site along α . Propagation runs for β vs β' , in Fig. 6, show a similar scenario. That is, a waterborne insonification of the bottom at $1\frac{1}{2}$ CZ occurs along β but not along β' . [One additional observation useful to understand-

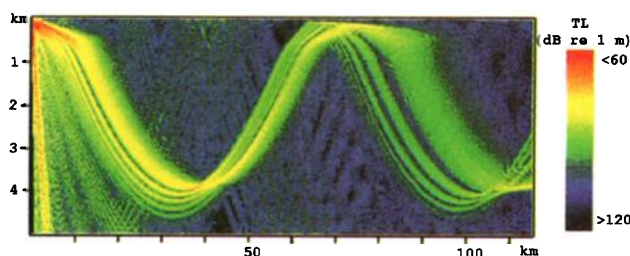


FIG. 4. Transmission loss (TL) for a range-independent cross section of the ocean using the sound-speed profile of Fig. 3 and the ten-element vertical source array shown in Fig. 2. Convergence zone structure typical of the region is evident as are sidelobes in the beampattern due to the untapered array, which is steered to 0° depression angle for this example. Modeling was done with the wide-angle PE.¹²

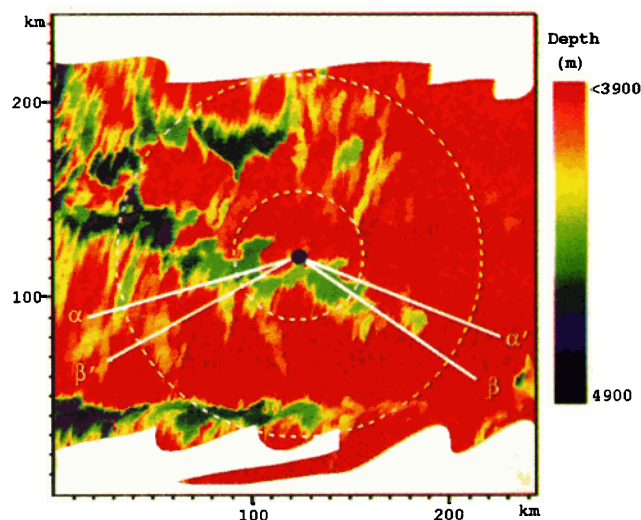


FIG. 5. Positive excess depth with respect to the conjugate depth of the source-array center. The white dotted lines indicate the approximate location of the source-beam vertex at $\frac{1}{2}$ and $1\frac{1}{2}$ CZ ranges from central observation R7E15 which is indicated by a dark dot. The solid white lines indicate radial pairs (α, α') and (β, β') symmetric about the array axis.

ing the backscatter process should be made. For each of the (α, α') and (β, β') runs presented in Fig. 6, backfacing scarps are generally insonified by the source beam while forward-facing scarps are in the acoustic shadow. Stronger backscatter is therefore expected from backfacing scarps.]

These examples illustrate the substantial differences in TL that can exist at ambiguous scattering sites due solely to asymmetry in bathymetry along ambiguous radials. In later sections we extend these results to objectively eliminate right-left ambiguity from backscatter data over wide areas by comparing TL at ambiguous scattering sites.

II. REVERBERATION MAPS

A. Data acquisition and reduction

Although a wide variety of waveforms were used during the ARC, from narrow-band continuous wave (cw) tonals to broadband hyperbolic frequency-modulated (hfm) emissions, we limit our present analysis to backscatter from cw signals of $\tau=2$ -s pulse duration. This is principally because the corresponding range resolution $\Delta r = c\tau/2 = 1.5$ km, for a nominal mean sound speed of $c=1.5$ km/s, is on the order of the cross-range resolution for the ranges relevant to the present study. (Cross-range resolution is simply the azimuthal resolution of the horizontal receiving array multiplied by the range of the scattering site.)

Azimuthal dependencies of the backscatter data are determined by beamforming time series data received on the array elements. Data were beamformed, filtered, and demodulated to a 128-Hz sample rate from the original rate of 2048 Hz. The data were then refiltered to within a 3-Hz band about the 270-Hz center frequency to eliminate out-of-band noise, leading to the beam-time format necessary for our mapping procedure.

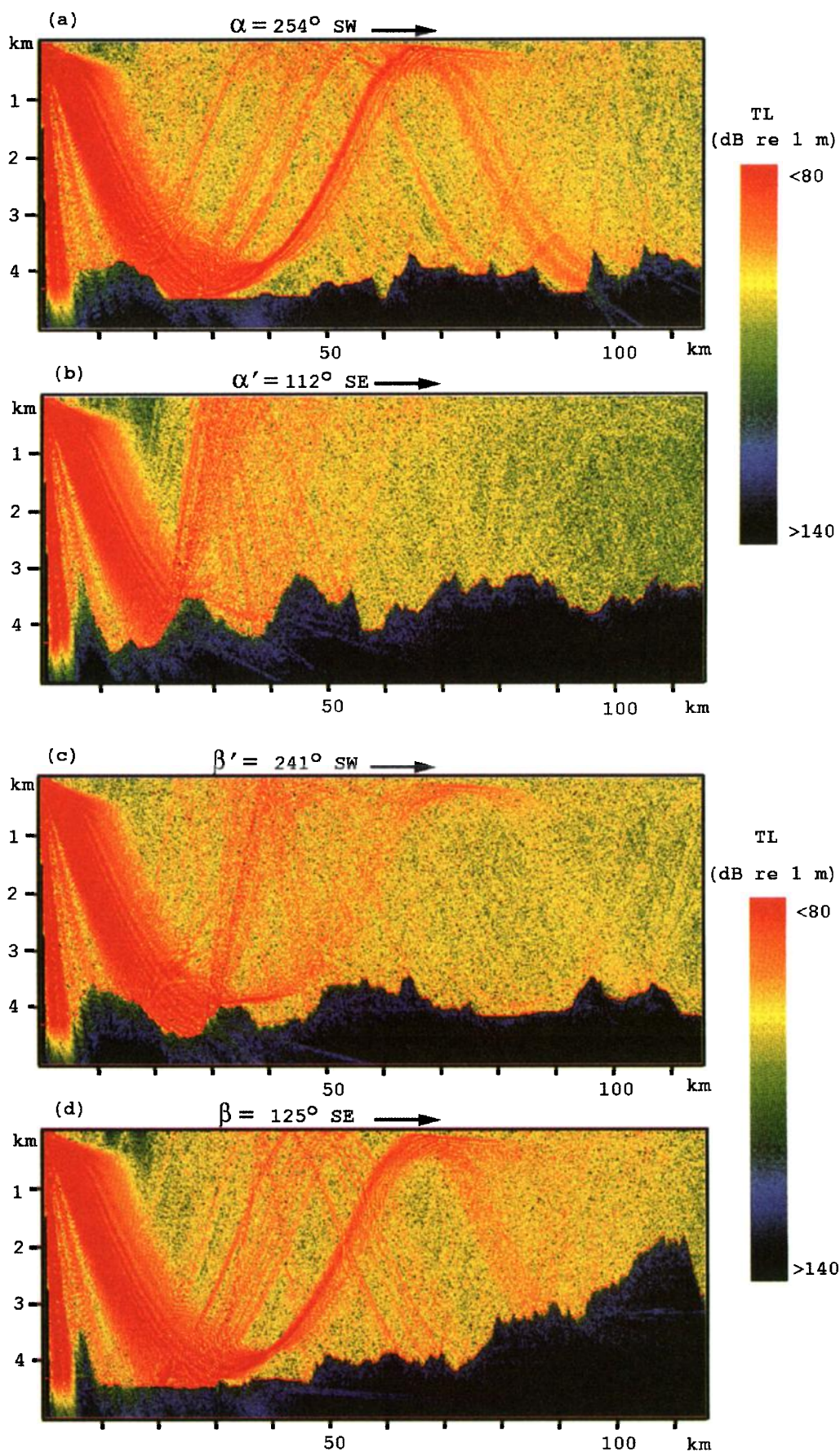


FIG. 6. Transmission loss (TL) for range-dependent cross sections of the ocean along the radials depicted in Fig. 5. In each case, propagation to $1\frac{1}{2}$ CZ is partially or fully blocked in the direct path for one member of each symmetric pair, and is clear for the other. (The source is modeled with the wide-angle PE as an untapered ten-element vertical array, shown in Fig. 2, steered to a 6° depression angle.) In general, backfacing scarps are insonified by the source beam while forward-facing scarps are in the acoustic shadow. Stronger backscatter is therefore expected from backfacing scarps.

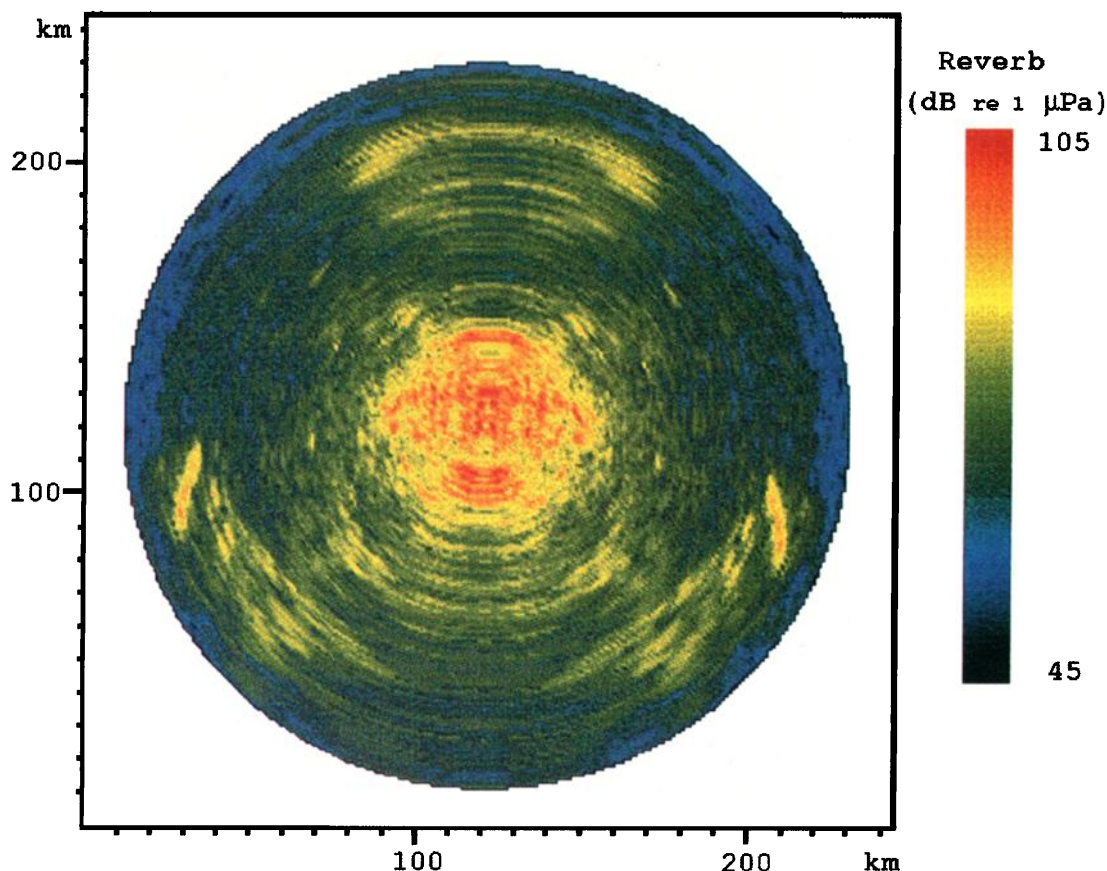


FIG. 7. A reverberation map for observation R7E15. Highest level returns occur within the direct path and at $\frac{1}{2}$ CZ range. All returns are mirrored about the array axis, roughly 183° azimuth, due to right-left ambiguity. Poor resolution due to endfire occurs within roughly $\pm 30^\circ$ of the array axis.

scatter, bathymetry, and TL. Referring to Fig. 6, backfacing scarps are insonified by waterborne paths at both sites α and β , while forward-facing scarps are in the acoustic shadow. The scarp at site α , where a broad backscatter return is charted, corresponds to the face of a prominent abyssal hill, while the scarps at β , where narrower returns are charted, belong to smaller ridges distributed on a shallower ledge.

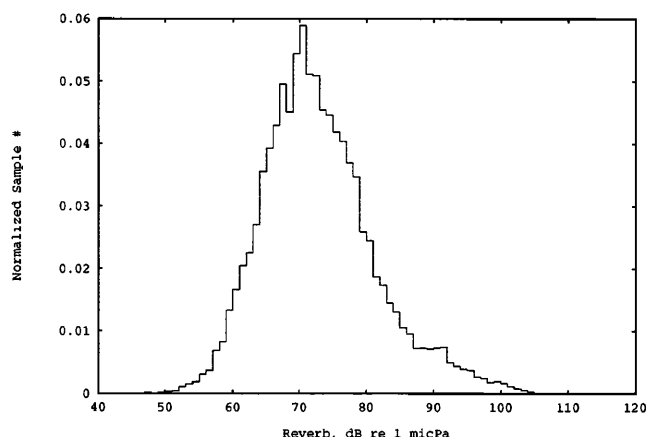


FIG. 8. A histogram of wide-area backscatter levels for observation R7E15 with mean level 73 dB re: 1 μ Pa, median 72 dB re: 1 μ Pa, and standard deviation 8.5 dB. Correcting for array gain and finite bandwidth, the noise floor corresponds to typical deep-ocean ambient noise levels.

III. TRANSMISSION LOSS MAPS

For comparison with reverberation, we are interested in the two-way TL, which is proportional to reverberation level R in the sonar equation

$$R = -TL_f - TL_b + S + 10 \log A + W, \quad (3)$$

where S is defined as scattering strength, W is the source strength, $A = r\Delta r\beta(\theta)$ is the scattering area, r is the range to the center of A , TL_f is the forward transmission loss from the vertical source array to bottom sites, and TL_b is the back transmission loss from bottom sites to the horizontal receiving array.

To map TL_f and TL_b over the wide areas surveyed in each backscatter observation, we extract bathymetry along $R=110$ -km radials at evenly spaced azimuthal increments $\Delta\theta=1^\circ$ about each observation. Along each radial, we compute the acoustic field in a two-dimensional range-depth cross section of the ocean using the wide-angle PE with the same frequency and environmental parameters used in Sec. I, Fig. 6. The TL at 1 m above the bottom (roughly $\lambda/6$) is extracted at evenly spaced ranges along each radial. For each observation, the radials are combined to produce a TL map over the entire survey area. To fill the areas between radials, the TL within $\pm\Delta\theta/2$ of each radial is given the value at the radial without interpolation. For TL_f we use the same vertical source array, steering, and normalization as in Fig. 6. For TL_b we use a point

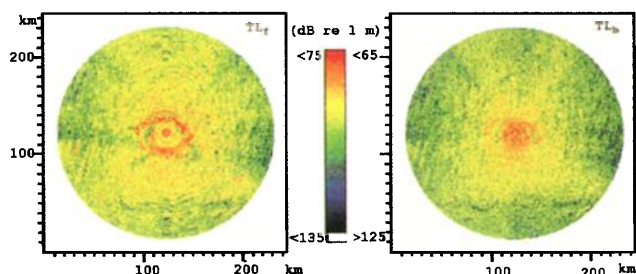


FIG. 9. Forward and back transmission loss maps TL_f and TL_b for observation R7E15. Modeling is done for radials at 1° increments. A general correspondence can be found between TL minima in these figures and backscatter maxima in Fig. 7.

source at the depth and central range of the horizontal receiving array and invoke reciprocity, with the understanding that variations in TL_b along the receiving array's aperture are negligible. Maps of TL_f and TL_b are shown in Fig. 9. While there is a general correspondence between the two maps, sharper features are found in TL_f due to the narrow beamwidth of the vertical array. This is especially so in the direct-path region where the incident field of the point source is more uniformly distributed on the ocean bottom.

The $TL_f + TL_b$ map for observation R7E15 is shown in Fig. 10. Direct-path and long-range sites insonified by waterborne paths have the lowest two-way TL. These occur within $\frac{1}{2}$ and at $1\frac{1}{2}$ CZ ranges, respectively, the latter being contingent upon the availability of a long-range propagation corridor. Two-way TL to sites at intermediate ranges is also low when the source beam is diverted by bottom interaction on the forward trip. However, bottom interaction on the return trip, which must occur by reciprocity, often causes a substantial increase in overall TL for such sites. If part of the source beam is rescattered into CZ propagation from these intermediate sites, its trajectory will not intersect the receiving array. Such redistribution of

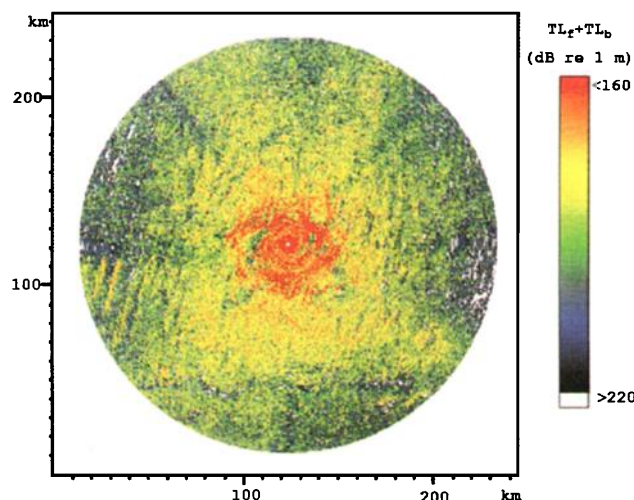


FIG. 10. Two-way transmission loss map of $TL_f + TL_b$ for observation R7E15. A general correspondence can be found between $TL_f + TL_b$ minima in this figure and backscatter maxima in Fig. 7.

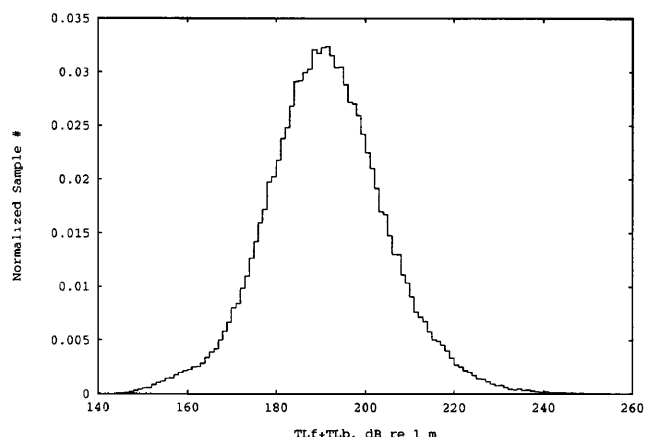


FIG. 11. A histogram of wide area $TL_f + TL_b$ for observation R7E15 with mean level 191 dB re: 1 m, median 191 dB re: 1 m, and standard deviation 14 dB. Two-way TL values corresponding to waterborne sites comprise the lower tail of this distribution.

acoustic energy is only of significance in bistatic observation geometries. Due to uncertainty in geoaoustic parameters of the seafloor, the level of modeled TL at intermediate sites insonified after previous source-beam bottom interaction is highly approximate. Since the angle of bottom reflection is primarily morphology related, the location of these intermediate sites is more dependable. For sites insonified by waterborne paths, which are more central to the analysis of this paper, knowledge of the geoaoustic parameters of the bottom is unnecessary for dependable TL modeling. While the corresponding reverberation map in Fig. 7 has ambiguities which smear and mirror the data about the array's axis, many features are closely matched by the two-way TL of Fig. 10.

The associated histogram in Fig. 11 shows a broad distribution of values with standard deviation significantly larger than that of the backscatter levels. Sites insonified by waterborne paths correspond to the lower tail of the distribution. Corresponding high-level backscatter occupies the upper tail of the distribution shown in Fig. 8. Like the histogram of backscatter level, the two-way TL distribution is also log normal, as is confirmed by the 0.98 normalized correlation coefficient obtained after cross correlation with a Gaussian distribution of the same mean and variance. Again, this is suggestive of an intermittent process, which for the TL case, can be readily attributed to the infrequent intersection of the source beam with the ocean bottom. The measurement of a log-normal distribution for backscatter level, Fig. 8, is consistent with the notion that two-way TL drives the level of backscatter.

To facilitate our comparison with measured backscatter, we incorporate the area term of the sonar equation by a running spatial integration of the antilog of negative two-way TL as windowed by the spatially varying resolution $r\Delta r\beta(\theta)$ set by the receiving array's beamwidth and waveform bandwidth. [We substitute the antilog of $TL_f + TL_b$ for $Ts(r, t)$ in Eq. (4) of Ref. 10.] This incorporates the area term of the sonar equation by effectively smearing the $TL_f + TL_b$ map to the resolution of the backscatter data

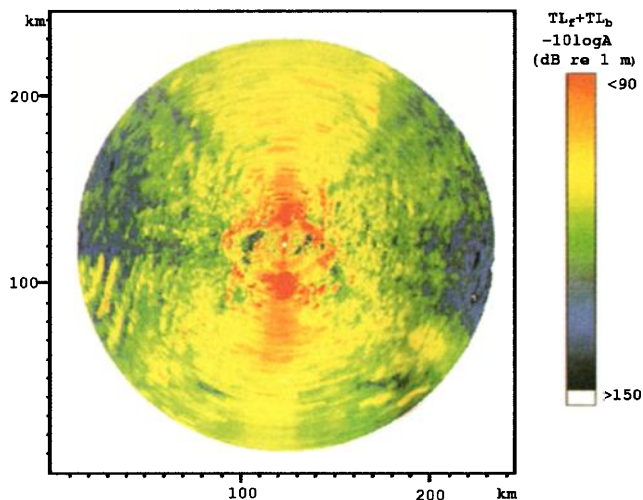


FIG. 12. A map of $TL_f + TL_b - 10 \log A$ for observation R7E15. The area term is incorporated by convolving the antilog of $-(TL_f + TL_b)$ with the spatially varying resolution window set by the receiving array's beamwidth and waveform bandwidth. Right-left ambiguity is not included. A general correspondence can be found between minima in this figure and backscatter maxima in Fig. 7.

without including right-left ambiguity, as is shown in Fig. 12. The new map is referred to as a $TL_f + TL_b - 10 \log A$ map.

It is now evident that TL selects the prominent fea-

tures found in the reverberation map. For example, at long range the lineated backscatter maxima at site α is precisely selected by an extended TL minima, confirming our previous deduction. The discrete returns associated with the waterborne path to site β , are also precisely selected by TL. Also, there is generally higher $TL_f + TL_b - 10 \log A$ to the west and east of the observation where correspondingly low backscatter is measured, partly due to the north-south orientation of the endfire beams.

While a broad azimuthal distribution of sites in the direct path have distinct TL minima, these are more difficult to compare with backscatter due to the excessive overlap of ambiguous returns. For comparative purposes, we have artificially applied right-left ambiguity to $TL_f + TL_b - 10 \log A$. [We substitute the antilog of the two-way TL for $f(r, t)$ and set $s(r, t) = 1$ in Eq. (5) of Ref. 10.] The result is shown in Fig. 13. A great similarity can now be seen between backscatter maxima and ambiguous $TL_f + TL_b - 10 \log A$ minima in the direct path, as well as at longer ranges where there is generally a pronounced $TL_f + TL_b - 10 \log A$ minima for every prominent backscatter maxima.

To quantify this comparison, we compute the normalized cross correlation between measured backscatter and modeled $TL_f + TL_b - 10 \log A$, shown in Figs. 7 and 13, respectively. We convert to linear units which are proportional to root-mean-square pressure and cross correlate

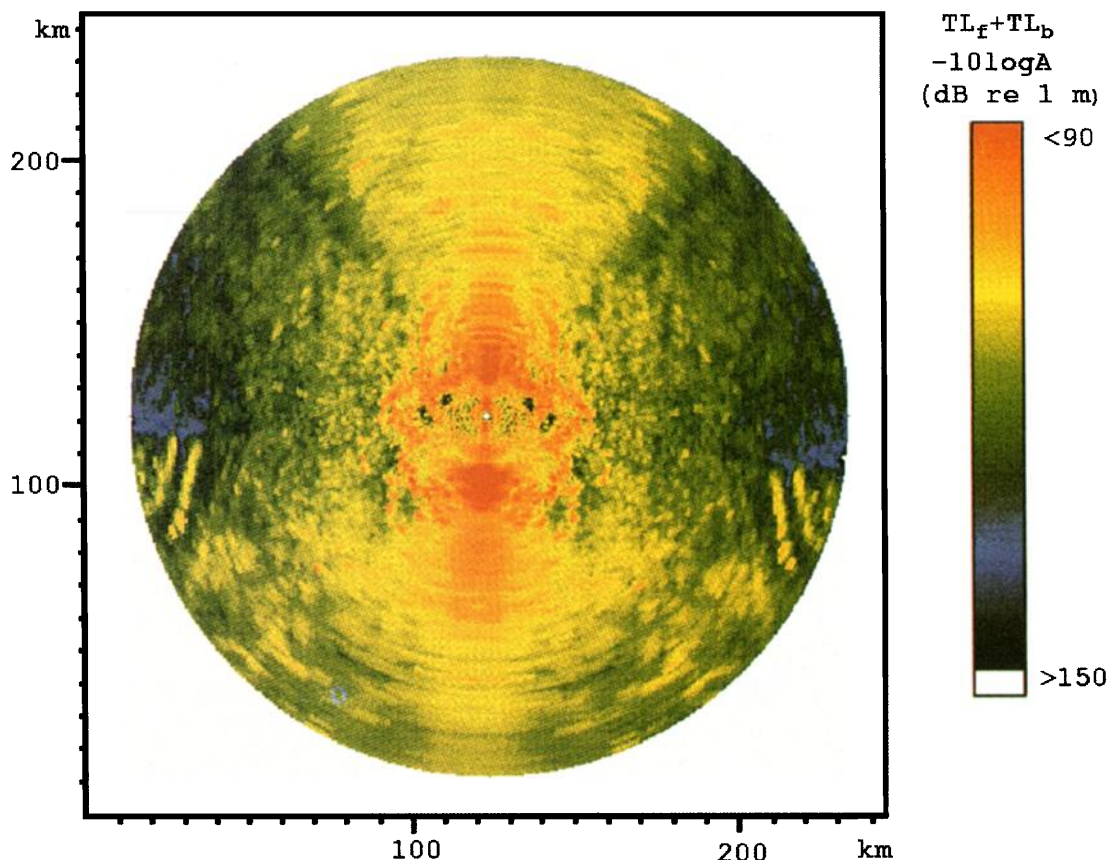


FIG. 13. Same as Fig. 13 except right-left ambiguity is now included. A general correspondence can be found between minima in this figure and backscatter maxima in Fig. 7. See Sec. III for quantitative cross correlation with backscatter.

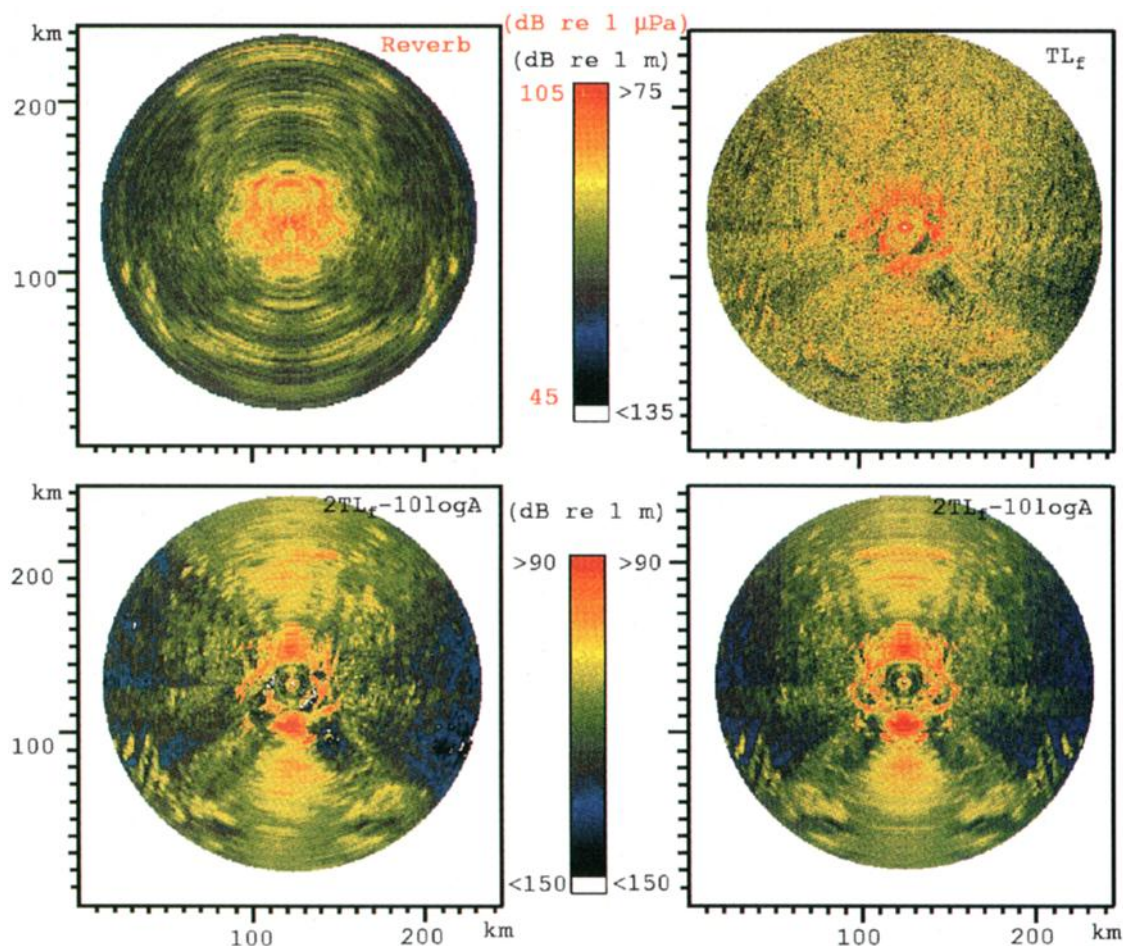


FIG. 14. Reverberation and TL_f maps for observation R7E10. We approximate $TL_f + TL_b$ by $2TL_f$ for R7E10, and again incorporate the area term by a running integration. Maps of $2TL_f - 10 \log A$ with and without ambiguity appear below. See Sec. III for quantitative cross correlation with backscatter.

$10^{R/20}$ with $10^{-(TL_f + TL_b - 10 \log A)/20}$. The rationale for this conversion is to first investigate correlation within the physical units of the problem. The resulting correlation coefficient is 0.59. However, there is also a strong physical motivation for correlating these quantities directly in decibels, as they are presented in the figures. Besides being linearly related in the sonar equation, our analysis shows that backscatter level R and two-way transmission loss $TL_f + TL_b$ have normal distributions. Since the cross-correlation function is a second moment characterization, its interpretation is unambiguous for variables which have normal distributions. That is, given a statistically significant number of samples, a high correlation unequivocally shows dependence while a low correlation shows independence for Gaussian variables. Therefore, the normalized correlation coefficient of 0.63 obtained after cross correlating R with $(TL_f + TL_b - 10 \log A)$ is not only quantitative, but unambiguous in demonstrating that spatial variations in charted backscatter are significantly dependent upon two-way transmission loss. Refinements in charting the backscatter as well as modeling the geoacoustic parameters of the bottom for TL computations will only improve the correlation.

At endfire, however, relative backscatter levels are lower than are predicted by modeled $TL_f + TL_b - 10 \log A$.

This is most likely due to the uniform spatial integration used in the modeling. Since the cross-range extent of end-fire sites generally exceeds the scale of geomorphological variation, discussed in the next section, significant scattering strength variation is likely within the spatial resolution of endfire sites. This could easily account for the noted difference.

We generate a TL_f map for observation R7E10, as shown in Fig. 14. Again, there is a strong correspondence with mapped reverberation, also shown in Fig. 14 for R7E10. In particular, the highest level backscatter features at $1\frac{1}{2}$ CZ are precisely selected by TL minima southwest of the observation position. This site is in the general vicinity of the elongated feature at site α in observation R7E15. However, the magnitude and shape of these returns varies significantly from R7E15. Since both observations were within 15 km ($\frac{1}{4}$ CZ) of each other, we conclude that small variations in measurement position can lead to large variations in the level of backscatter at a given site. To facilitate qualitative comparison with backscatter, we approximate $TL_f + TL_b$ by $2TL_f$ for R7E10, and again incorporate the area term by a running integration. The result is also shown in Fig. 14 for unambiguous and ambiguous cases respectively, where $2TL_f - 10 \log A$ is higher than $TL_f + TL_b - 10 \log A$ within the direct path due to

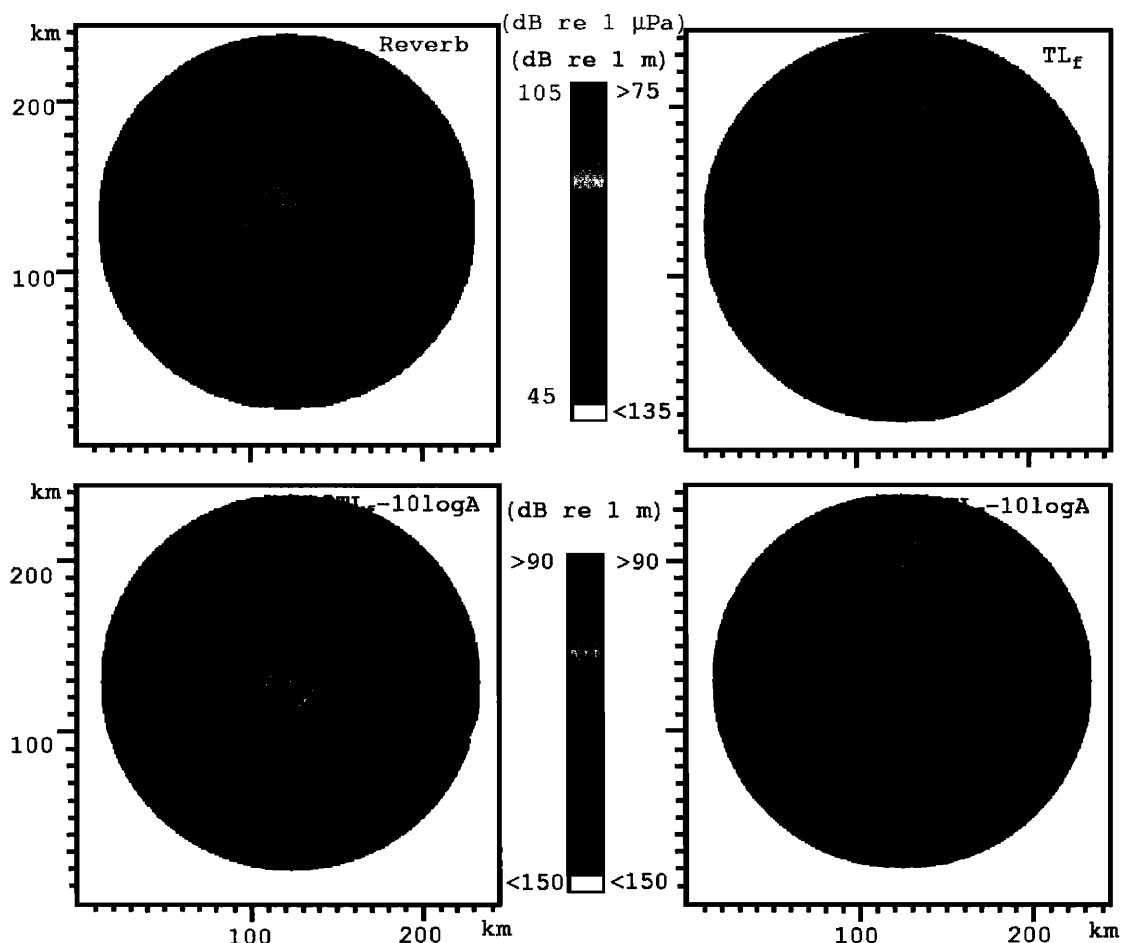


FIG. 14. Reverberation and TL_f maps for observation R7E10. We approximate $TL_f + TL_b$ by $2TL_f$ for R7E10, and again incorporate the area term by a running integration. Maps of $2TL_f - 10 \log A$ with and without ambiguity appear below. See Sec. III for quantitative cross correlation with backscatter.

$10^{R/20}$ with $10^{-(TL_f + TL_b - 10 \log A)/20}$. The rationale for this conversion is to first investigate correlation within the physical units of the problem. The resulting correlation coefficient is 0.59. However, there is also a strong physical motivation for correlating these quantities directly in decibels, as they are presented in the figures. Besides being linearly related in the sonar equation, our analysis shows that backscatter level R and two-way transmission loss $TL_f + TL_b$ have normal distributions. Since the cross-correlation function is a second moment characterization, its interpretation is unambiguous for variables which have normal distributions. That is, given a statistically significant number of samples, a high correlation unequivocally shows dependence while a low correlation shows independence for Gaussian variables. Therefore, the normalized correlation coefficient of 0.63 obtained after cross correlating R with $(TL_f + TL_b - 10 \log A)$ is not only quantitative, but unambiguous in demonstrating that spatial variations in charted backscatter are significantly dependent upon two-way transmission loss. Refinements in charting the backscatter as well as modeling the geoacoustic parameters of the bottom for TL computations will only improve the correlation.

At endfire, however, relative backscatter levels are lower than are predicted by modeled $TL_f + TL_b - 10 \log A$.

This is most likely due to the uniform spatial integration used in the modeling. Since the cross-range extent of end-fire sites generally exceeds the scale of geomorphological variation, discussed in the next section, significant scattering strength variation is likely within the spatial resolution of endfire sites. This could easily account for the noted difference.

We generate a TL_f map for observation R7E10, as shown in Fig. 14. Again, there is a strong correspondence with mapped reverberation, also shown in Fig. 14 for R7E10. In particular, the highest level backscatter features at $\frac{1}{2}$ CZ are precisely selected by TL minima southwest of the observation position. This site is in the general vicinity of the elongated feature at site α in observation R7E15. However, the magnitude and shape of these returns varies significantly from R7E15. Since both observations were within 15 km ($\frac{1}{4}$ CZ) of each other, we conclude that small variations in measurement position can lead to large variations in the level of backscatter at a given site. To facilitate qualitative comparison with backscatter, we approximate $TL_f + TL_b$ by $2TL_f$ for R7E10, and again incorporate the area term by a running integration. The result is also shown in Fig. 14 for unambiguous and ambiguous cases respectively, where $2TL_f - 10 \log A$ is higher than $TL_f + TL_b - 10 \log A$ within the direct path due to

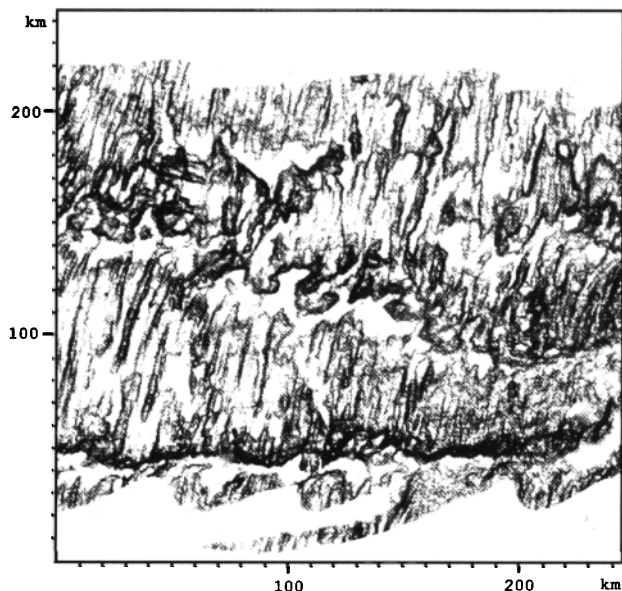


FIG. 15. Lambertian shaded bathymetric relief for a light source centered above the region at infinity. Site α corresponds to a typical abyssal hill, and β to a shallow ledge on the Mid-Atlantic Ridge.

the above approximation. A normalized correlation coefficient of 0.54 is measured between backscatter level R and the combined transmission loss-area terms of the sonar equation $-(TL_f + TL_b - 10 \log A)$ for observation R7E10. Converting to linear units as before, the correlation coefficient is 0.47. These results are consistent with those obtained for observation R7E15.

In summary, we find that the level of backscatter is strongly dependent upon TL. Two-way TL selects the sites from which high-level backscatter is returned, with backscatter maxima corresponding to TL minima. Small variations in measurement position, less than $\frac{1}{4}$ CZ, can lead to large variations in the level of backscatter returned from a given site due to bathymetry related variations in TL. Larger variations in measurement position can also lead to spatial variations in backscatter. However, these may simply be due to shadow zones associated with CZ propagation, and are not necessarily bathymetry related.

IV. WESTERN MID-ATLANTIC RIDGE GEOMORPHOLOGY

A. Bathymetry and geomorphology

Two well-defined corridors of excess depth run across the survey area, as is evident in Figs. 1 and 5. These are often referred to as "segment valleys" or "fracture zones" since they are caused by separation of the local plate segment. They are best seen in Fig. 15 where depth perspective is simulated by artificially shading the bathymetry as a Lambertian surface with a light source at infinity directly above center. Darker shading indicates steeper slope. The lower segment valley runs east-west along the very bottom of the image. The central segment valley follows a more circuitous southeast to northwest route. Ridge boundaries found on the northern edge of the central segment valley

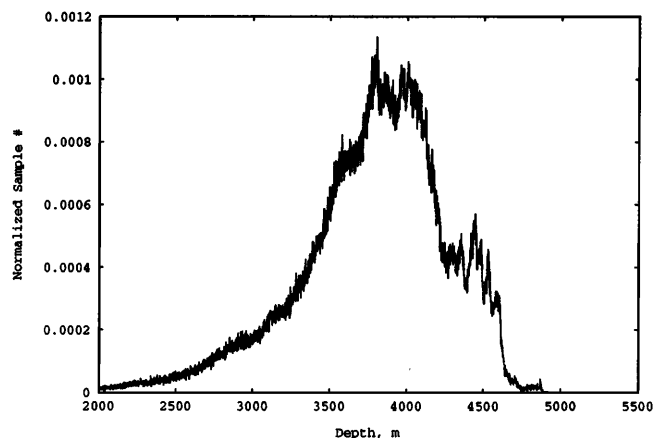


FIG. 16. A histogram of bathymetry intersecting the circular region surveyed by backscatter data in Fig. 7, with mean depth 3785 m, median depth 3833 m, and standard deviation 467 m.

are believed to be geologically distinct from those found on southern edge. Northern ridge boundaries are known as "inside corners" and have irregular morphology. Southern ridge boundaries are known as "outside corners" and have more regularly lineated tendencies typical of abyssal hills. "Compared to outside corners, inside corners have excess elevation, high-residual gravity anomaly, steep and often irregularly oriented slopes created by multiple high angle faults..."^{18,19} Away from fracture zones, ridges tend to have axes parallel to the MAR, extending from North to South. They also tend to be distributed regularly with a spatial period of about 5 km. (The faint diagonal striations throughout the shaded bathymetry at about 20° inclination from horizontal are an artifact of the data acquisition. Their pattern is related to the swaths covered by the research vessel.) A histogram of the depth distribution for the entire survey area is presented in Fig. 16. The mean depth is within a standard deviation of the conjugate depth, insuring the extensive bottom interaction discussed in previous sections.

B. Directional derivatives of bathymetry

We are also interested in the relationship between reverberation and seafloor slope. For example, does high-level backscatter return predominantly from steep slopes? If so, is it biased toward slopes facing the observation position? To study this we have computed a directional derivative (DD) of the bathymetry by taking the dot product of the gradient vector with a unit vector pointing in the direction of observation R7E15 from the given field point. This is useful since it gives an overview of the vertical slopes encountered on a path radially outward from the source, as sound travels. A spatial map of DD can be used to detect the horizontal orientation of ridges with vertical slopes facing the observation position. The result is shown in Fig. 17. Since the gradient is computed by finite differences, the DD resolution is no finer than the 200-m grid interval of the bathymetry.

Here we identify ridges as lineations of high DD magnitude. For a given ridge, surfaces facing the observation

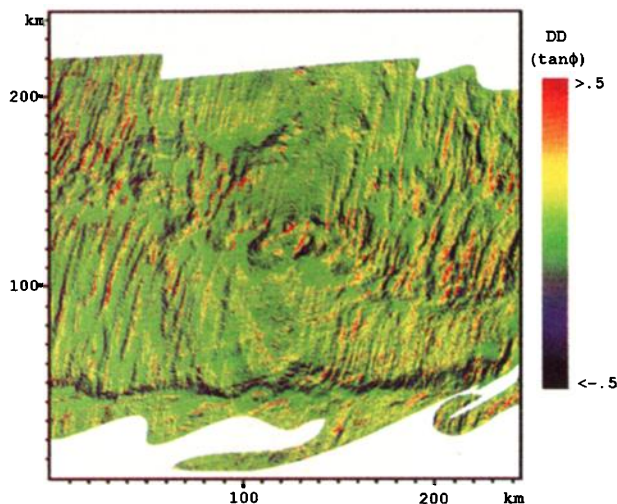


FIG. 17. A directional derivative (DD) of the bathymetry equal to the dot product of the gradient vector at each point in the field with the unit vector pointing from the location of observation R7E15. This gives the slope orientation along the path sound waves travel from the source. Positive values indicate slopes facing the observation (back facing), and negative values indicate slopes facing away (forward facing). Slopes are given by $\tan \phi$, where ϕ is the slope angle from horizontal along the DD.

point have positive DD, surfaces facing away have negative DD, and surfaces normal have zero DD. Since the ridge axes generally run north-south, we often find north-south lineations of high DD magnitude east and west of the observation point corresponding to abyssal hills. To the north and south, ridge axes are generally parallel to the observation direction where we find DD maxima diffusely distributed in speckled patterns corresponding to ridge edges and crests. These patterns are better defined at segment valley walls along the fracture zone central to the observation, and are most coherent for the irregularly shaped inside corners which give much higher DD values than outside corners, as is anticipated. Abyssal and segment valley floors tend toward zero slope.

A histogram of the DD distribution for the survey area is presented in Fig. 18 where a sharply peaked and symmetric distribution with 8° variance about zero slope is found. Slopes facing the observation position are as likely to be found along a propagation radial as slopes facing away. However, tails of the distribution beyond $\pm 25^\circ$ are not accurate. This is due to limitations of the measurement system and coarseness of the sampling interval.

To obtain a quantitative estimate of the scales over which bathymetry varies, we have computed the wave-number spectrum, shown in Fig. 19. The dominant spectral component is in the low wave-number regime corresponding to length scales greater than about 5 km. Variations within the array's range resolution (1.5 km) are less significant on average. However, from the DD map in Fig. 17, steep slopes do exist within these smaller scales. While they are less frequently encountered, steep slopes associated with lineated ridges are more likely to terminate shallow-angle propagation, typical at long ranges, than level areas which tend to occur in valleys below the conjugate depth contour. High wave number spikes of roughly

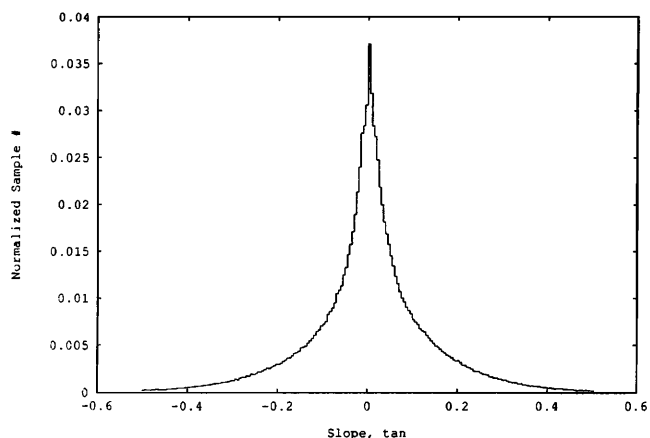


FIG. 18. A histogram of DD intersecting the circular region surveyed by backscatter data in Fig. 7, with mean slope 0.20° , median 0.23° and standard deviation 8.0° from horizontal. Slopes near zero predominate, and neither slopes facing or opposing the observation are favored.

20 dB occur for spatial frequencies greater than 1 km^{-1} . These are an artifact of registration error along neighboring measurement swaths and do not reliably correspond to actual bathymetric variations.

V. COMPARISONS WITH BATHYMETRY

To correlate backscatter with geomorphology, a color reverberation map is projected onto the black and white shaded bathymetry relief. The resulting image is presented in Fig. 20 for observation R7E15. To insure that bathymetric variations are not obscured in the relief, only high level backscatter is presented.

While cross-range smearing and right-left ambiguity make the image somewhat confusing, close inspection re-

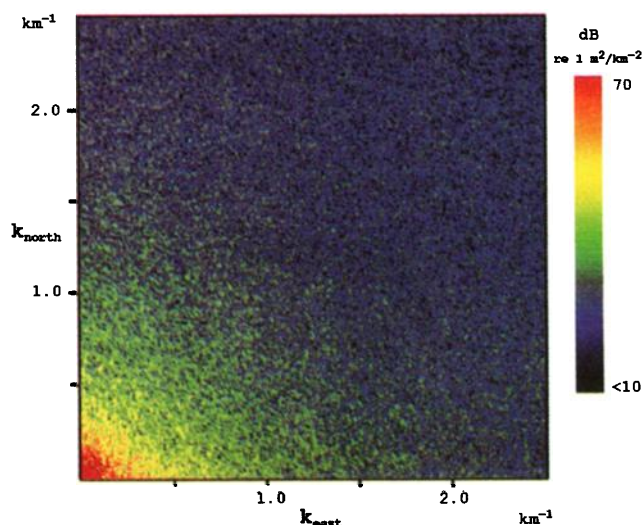


FIG. 19. A two-dimensional wave number spectrum of hydrosweep bathymetry over a $102.4 \times 102.4 \text{ km}^2$ spatial window within the region shown in Fig. 1. The dominant spectral components occur for length scales greater than about 5 km. High wave-number spikes of roughly 20 dB occurring for spatial frequencies greater than 1 km^{-1} do not correspond to actual bathymetric variations. These are an artifact of registration error along neighboring measurement swaths of the bathymetry.

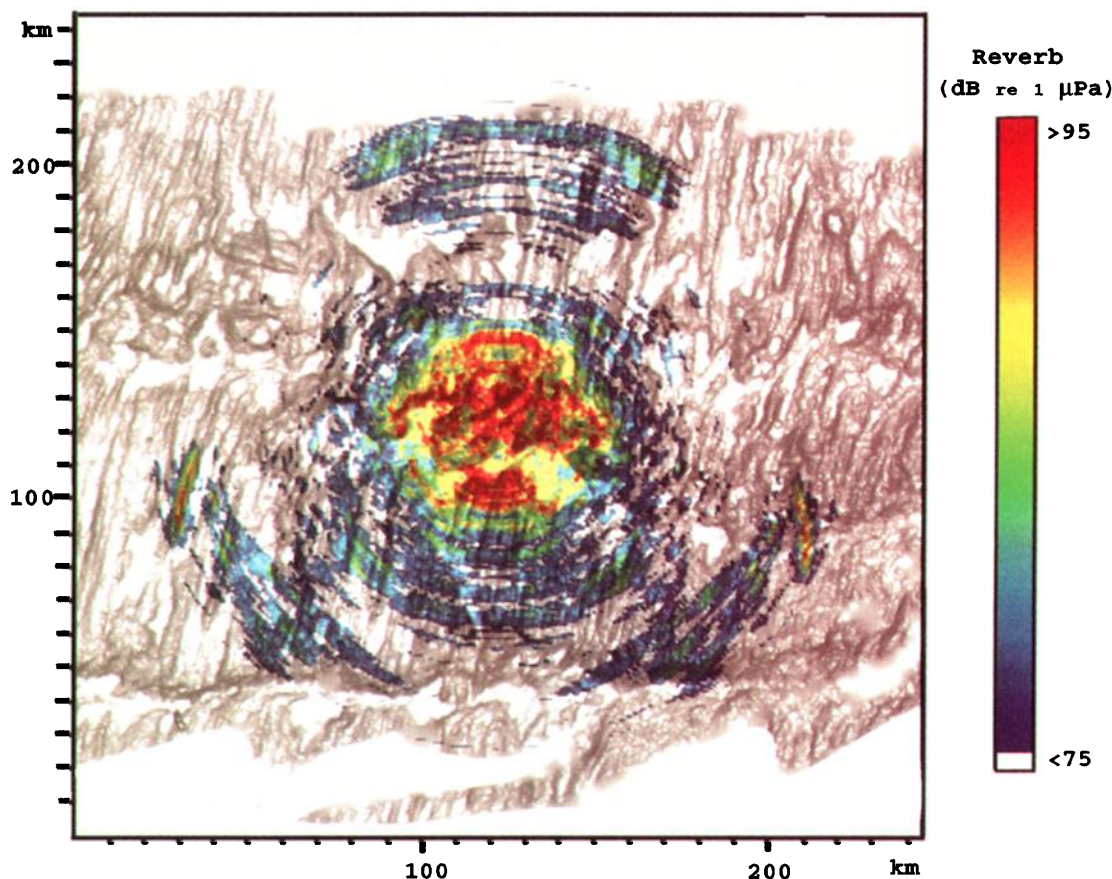


FIG. 20. Color backscatter levels from observation R7E15 projected onto corresponding Lambertian shaded bathymetry, see Fig. 16. Right-left ambiguity has not been eliminated. Higher level backscatter returns often resemble the bathymetric features to which they are mapped. Only prominent backscatter is shown to avoid obscuring bathymetric variations.

veals that many high-level backscatter features closely match corresponding bathymetry. However, we do not base our distinction between true and virtual scattering sites upon visual correlation. While this method may often be accurate, as well as intuitive, the probability of false correlation is also high given cross-range resolution which is often only slightly less than the separation between ridges.

Instead, we resolve right-left ambiguity by comparing $TL_f + TL_b - 10 \log A$ at ambiguous scattering sites. If the difference in $TL_f + TL_b - 10 \log A$ is greater than a chosen threshold, we associate the true scattering site with the place of lower $TL_f + TL_b - 10 \log A$ and map the corresponding backscatter levels to this site. If the difference is less than this threshold we do not make a distinction, and project backscatter level onto neither site. We choose a threshold of 10 dB which constitutes a significant enough difference in $TL_f + TL_b - 10 \log A$ to rule out false identification in most cases.

The resulting unambiguous backscatter levels are projected onto shaded bathymetry and presented in Fig. 21 for observation R7E15. Again, only high-level backscatter (> 70 dB re: $1 \mu\text{Pa}$) is presented to insure that bathymetric variations are not obscured. We first note that folding the figure about the array's axis yields the same prominent returns depicted in the ambiguous Figs. 7 and 20. In other

words, little information about high-level backscatter is lost by the choice of a 10-dB threshold. On the other hand, a general correspondence between prominent bathymetry and high-level backscatter is now evident. In particular, the backscatter lineation at site α discussed in previous sections corresponds to an abyssal hill to the southwest of the observation. The well-defined pattern of high-level backscatter found in the direct path traces the ridge contours surrounding the segment valley which runs central to the observation position.

The relationship between prominent backscatter and the ridge structure is further elucidated in Fig. 22 by overlay on a DD map. Here prominent returns can be more easily associated with specific ridges. For example, this is the case within the direct path, as well as at long-range sites α and β . However, it is also evident that the resolution window is frequently wider than scarps within the ridges. That is, returns are typically mapped to areas larger than the width of associated scarps. As a result, quantitative comparisons between slope orientation and backscatter are not possible with the given measurements, and are left for future analysis with higher resolution data. (Preliminary results from high resolution measurements made during the main acoustics experiment show a strong relationship between backfacing scarps and backscatter.²⁰)

However, an association between backfacing scarps

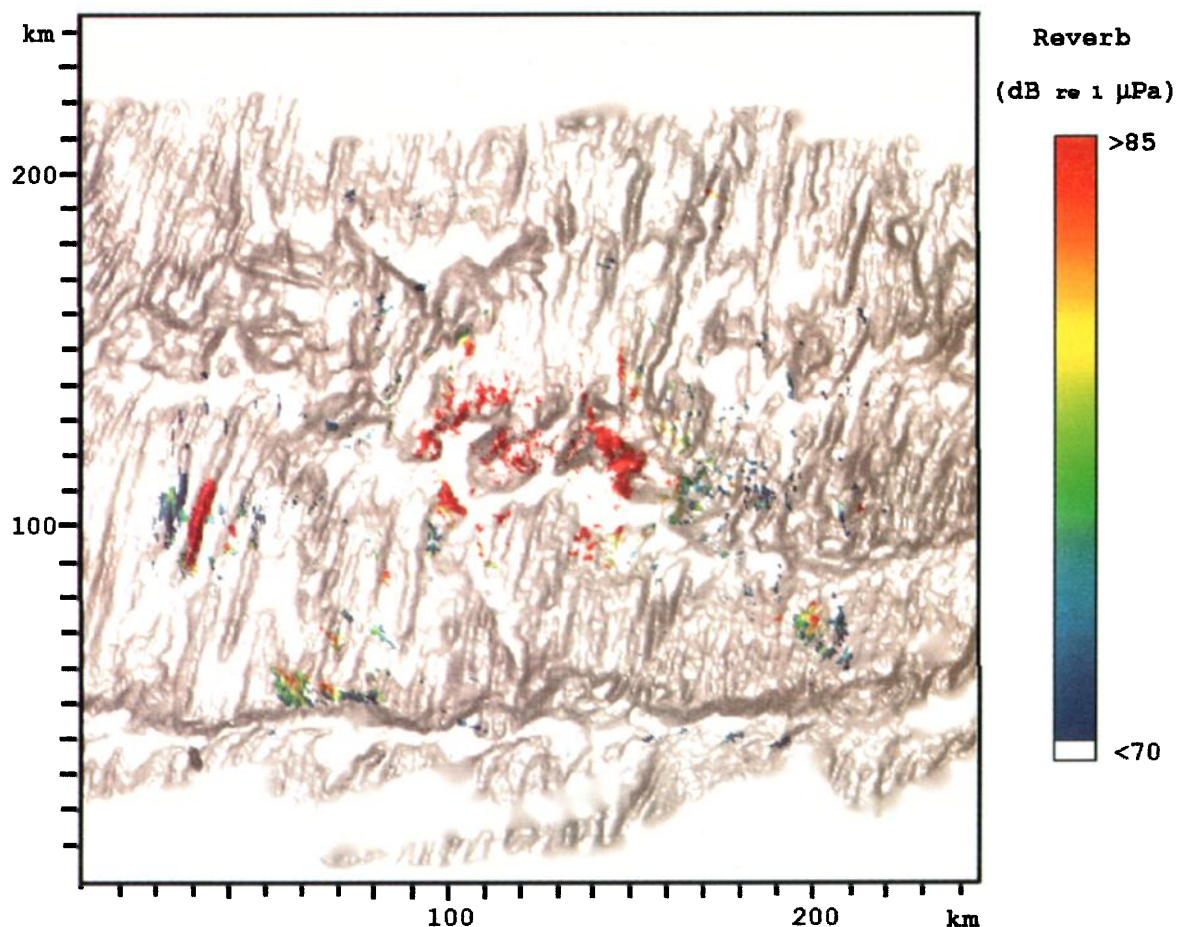


FIG. 21. Same as Fig. 20 except ambiguity has been eliminated with a TL-based environmental symmetry breaking technique. Only prominent backscatter is shown to avoid obscuring bathymetric variations. Highest level backscatter is found where waterborne paths are available. Well-defined patterns in backscatter often correspond to bottom morphology, following ridges protruding above the conjugate depth contour.

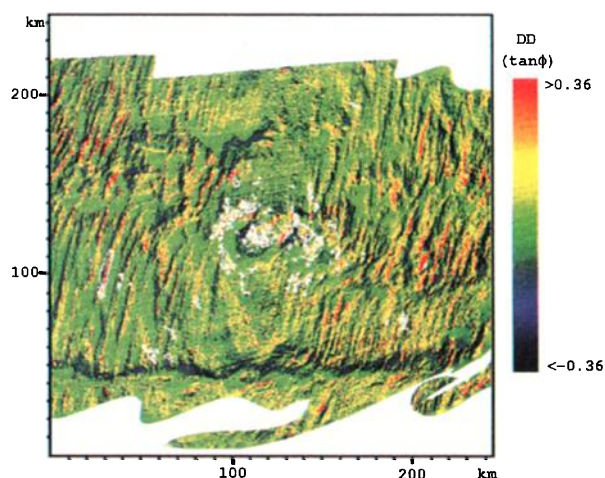


FIG. 22. White contours of unambiguous backscatter exceeding 80 dB re: 1 μ Pa are projected onto the color map of DD shown in Fig. 17. Well-defined patterns in backscatter often follow ridges with extended back-facing scarps. Backscatter resolution for the given signal is generally too poor resolve the scarps.

and prominent backscatter can still be made in the present study with the aid of the TL modeling presented in Secs. I and III. Specifically, the resemblance between high-level backscatter and bathymetry can be largely attributed to spatial variations in TL. We focus on the numerous sites which are insonified by waterborne paths and therefore return the most prominent backscatter. This is because there is little question regarding the wide-angle PEs accuracy in modeling TL along waterborne paths for a range-independent water column in the deep ocean. For example, compare the TL maps in Figs. 10 and 12 with the bathymetric maps shown in Figs. 1, 5, 15, and 17. Within the direct-path, segment valley ridges facing observation R7E15 are broadly outlined by TL minima along the conjugate depth contour. And, lineations of minimum TL occur at $1\frac{1}{2}$ CZ ranges on backfacing scarps for ridges which protrude above the conjugate depth contour over a wide azimuth, as is the case at site α . In general, ridges which cross the propagation path are more likely to show up as TL lineations since they span broader azimuthal sectors than those running parallel to the propagation path. As a consequence of the predominantly north-south running ridge axes of the western MAR, ridges east and west of the observation are more likely to yield backscatter lineations.

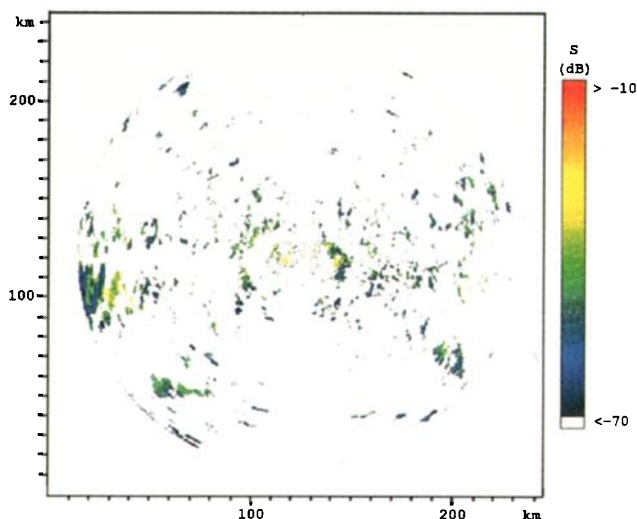


FIG. 23. Scattering strength over a wide-area for observation R7E15. The estimate is based upon the unambiguous backscatter levels, see Fig. 21 and caption, and the unambiguous $TL_f + TL_b - 10 \log A$ levels presented in Fig. 12 for a 233 dB *re*: 1 μ Pa and 1-m source strength.

VI. SCATTERING STRENGTH

We estimate scattering strength S over a wide area by adding unambiguous backscatter level R to modeled $TL_f + TL_b - 10 \log A$ and subtracting the source strength $W = 233$ dB *re*: 1 μ Pa and 1 m. The result appears in Fig. 23 for observation R7E15 where we find uniformly low scattering strength values. (Here we have used the full range of unambiguous backscatter levels as opposed to just the prominent values overlain on relief bathymetry in Fig. 21.) A histogram is shown in Fig. 24 where scattering strength is distributed narrowly about the median, roughly following the anticipated log-normal distribution found in backscatter level and transmission loss. A 0.96 normalized correlation coefficient is obtained after cross correlation with a Gaussian distribution of the same mean and variance. The low variance and generally uniform spatial dis-

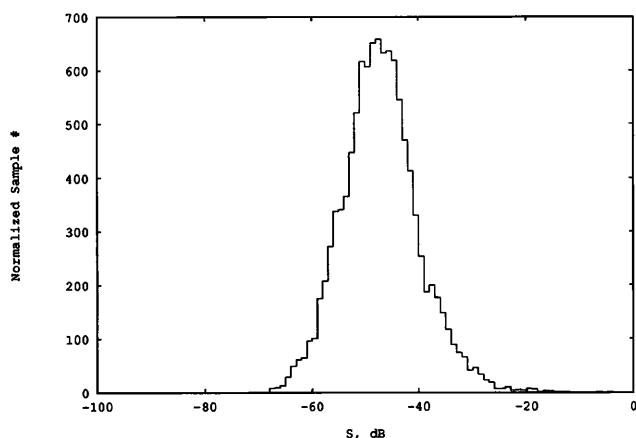


FIG. 24. A histogram of the scattering strength values at sites presented in Fig. 23, with mean -47 dB, median -47 dB and standard deviation 7 dB. Since the signal used cannot resolve distinct bathymetric features which may dominate the backscatter process, these statistics are primarily useful as a lower bound for the survey area.

tribution of scattering strength is consistent with the low resolution of the measurement. That is, contributions from elemental scatterers are well mixed in the long-range, low-resolution backscatter returns.

The scattering strength values presented are useful as a lower bound for the region. This is because the backscatter data presented cannot resolve the dominant contributors, as is suggested in the previous section. Since these contributors are under-resolved, their scattering strength is likely underestimated. (As a point of interest, we note that the lower bound measured, 47 ± 4 dB is roughly consistent with Lambert's law $S = 20 \log(\sin \psi) - \mu$ and the Mackenzie coefficient $\mu = -27$ dB (Ref. 21) for the predominantly shallow grazing angles, $\psi < 10$, of this survey. However, we believe that this result is merely coincidental. Recent work with high-resolution FM signals in the same area indicate that actual scattering strengths are significantly higher.^{16,22)}

VII. CONCLUSIONS

Two primary conclusions are drawn from this initial analysis of long-range backscatter in the western MAR: (a) there is a high correlation between prominent backscatter and detailed bottom morphology; (b) the range and azimuth of prominent backscatter can be determined by propagation modeling if high-resolution bathymetry is available. In general, measured backscatter maxima correspond to modeled transmission loss (TL) minima when charted to respective locations on the sea floor. These spatial extrema are most pronounced in the direct path and at $n + \frac{1}{2}$ CZ ranges when propagation is not blocked at shorter range for the given azimuth, where $n = 0, 1$ for the present study. At these ranges, backscatter maxima typically follow extended ridges along the local conjugate depth contour. This is partially explained by propagation modeling which shows that forward propagation paths tend to insonify the backfacing scarps along ridges which protrude above the conjugate depth contour. This leads to the corresponding TL minima which apparently play a fundamental role in driving the level of backscatter. Whether the prominence of these returns is also related to scattering properties of the associated ridges and their orientation is still uncertain. This uncertainty arises because the resolution of the measurements presented in this study is often too poor to adequately resolve the scarps, let alone more elementary contributors to the scattering process which may reside within the scarps.

Although we do not yet fully understand the scattering process, we have learned a great deal about reverberation. Our analysis has provided a simple method of forecasting the range and azimuth of prominent backscatter in the MAR. Either by a crude tracing of CZ circles on an excess depth map, or a more accurate modeling of transmission loss with a full-wave propagation model such as the wide-angle PE. Both of the above methods were used in designing the main acoustics experiment of the SRP. The preliminary results of this more recent experiment show that both methods are extremely dependable in forecasting prominent backscatter in the MAR.^{20,23}

We have also estimated scattering strength over a wide area and have obtained a lower bound of -47 ± 4 dB for the survey. Our estimates provide a lower bound because well-defined morphological features, which apparently play a major role in the backscatter process, are under-resolved by the cw measurements used in this study. More recent scattering strength estimates made with much higher resolution FM data have yielded significantly higher values for the same region.²² Nevertheless, the estimates presented here show a low variance and generally uniform spatial distribution. This is consistent with the high cross correlation measured between long-range backscatter and TL in this study. Evidently, distinct scattering contributors are so well mixed in the large areas integrated by long-range returns that the most significant variations in backscatter are generally due to propagation. This further supports the idea of backscatter forecasting by propagation modeling. It also suggests that the possibility of remote bathymetric survey by backscatter measurement^{5,6,24} is practical. However, a more negative implication is that any of a number of scattering models will be able to match long-range MAR backscatter data, regardless of whether they are correct, so long as a sufficient propagation model is used.

Investigations into the fundamental scattering process are better suited to the site-specific Main Acoustics Cruise of July 1993. This bistatic experiment was designed specifically around three sites detailed in the hydrosweep bathymetry. High-resolution monostatic and bistatic reverberation measurements were made at various ranges and orientations from known scarps. Short-range measurements should enable resolution of distinct small-scale contributors to the scattering process. While, long-range measurements will show how these accrue in distant reverberation. Vertical arrays were also deployed before select backfacing scarps to explore the vertical structure of the scattered field near the scatterers. These data are to be compared with hydrosweep as well as finer scale bathymetry and geological data recently collected to further elucidate the scattering process. In addition, tow-ship tracks in the Main Acoustics Experiment were designed with ambiguity removal as an essential theme. Star patterns rather than polygons were used extensively to provide redundant measurements at differing array headings at a point of convergence. This was necessary because the present study has shown that small differences in measurement position, as small as CZ/4, can lead to drastic differences in backscatter due to bathymetry related variations in TL. Preliminary results from the '93 cruise indicate that the environmental symmetry breaking technique for ambiguity removal presented here is consistent with ambiguity removal by comparison of data from multiple adjacent array headings.²⁰ A detailed report on these results is in preparation.²³

ACKNOWLEDGMENTS

This work has benefited greatly from discussions with and assistance from our NRL colleagues Michael Collins, Dalcio Dacol, Gary Gibian, Timothy Krout, William Kuperman, Richard Menis, Gary Murphy, Peter Ogden,

Bruce Palmer, John Perkins, and Peter Vogt. We would also like to thank the members of the SRP community for many useful discussions and insights. In particular we thank the ARSRP chief scientist John Orcutt of SIO for his encouragement, and Brian Tucholke of WHOI for making the SRP hydrosweep bathymetry available. This work was made possible by partial support from our sponsors at ONR, Mohsen Badiey and Marshall Orr.

- ¹ A. B. Baggeroer and J. Orcutt, "Overview of the ONR Reconnaissance Cruise for the Acoustic Reverberation Special Research Program," in *Ocean Reverberation*, edited by D. Ellis, J. Preston, and H. Urban (Kluwer, Dordrecht, 1993).
- ² J. M. Berkson, N. C. Makris, R. Menis, T. L. Krout, and G. L. Gibian, "Long-range measurements of sea-floor reverberation in the Mid-Atlantic Ridge area," in *Ocean Reverberation*, edited by D. Ellis, J. Preston, and H. Urban (Kluwer, Dordrecht, 1993).
- ³ Bathymetry data were acquired by the Hydrosweep 15-kHz multi-narrow-beam echosounding system from the R/V Ewing. Brian E. Tucholke from the Woods Hole Oceanographic Institution was the Principal Investigator, Martin C. Kleinrock and Jian Lin also from the Woods Hole Oceanographic Institution were Co-principal investigators.
- ⁴ R. C. Spindel and J. R. Heirtzler, "Long-Range Echo Ranging," *J. Geophys. Res.* **77**, 7073–7078 (1972).
- ⁵ D. E. Shifter, E. R. Franchi, J. M. Griffin, and B. B. Adams, "Hydrographic Reconnaissance of Large Undersea Topography using Scattered Energy," in *Rec. 1980 IEEE Electron. Aerospace Syst. Conventions*, 270–274 (1980).
- ⁶ F. T. Erskine, G. M. Bernstein, S. M. Brylow, W. T. Newbold, R. C. Gauss, E. R. Franchi, and B. B. Adams, "Bathymetric Hazard Survey Test (BHST Rep. No. 3), Scientific Results and FY 1982–1984 Processing," *NRL Rep.* 9048 (1987).
- ⁷ J. M. Berkson and T. Akal, "Simultaneous Reception of Long-Range Long-Frequency Backscattered Sound by a Vertical and Horizontal Array," *IEEE J. Ocean. Eng.* **OE-12**, 362–367 (1987).
- ⁸ J. R. Preston, T. Akal, and J. M. Berkson, "Analysis of backscattering data in the Tyrrhenian Sea," *J. Acoust. Soc. Am.* **87**, 119–134 (1990).
- ⁹ L. Nghiem-Phu and F. Tappert, "Parabolic equation modeling of bottom reverberation using seafloor roughness spectra," *J. Acoust. Soc. Am. Suppl.* **1** 88 (1990).
- ¹⁰ N. C. Makris, "Imaging ocean-basin reverberation via inversion," *J. Acoust. Soc. Am.* **94**, 983–993 (1993).
- ¹¹ R. A. Wagstaff, M. R. Bradley, and M. A. Herbert, "The Reverberation Array Heading Surface," in *Ocean Reverberation*, edited by D. Ellis, J. Preston, and H. Urban (Kluwer, Dordrecht, 1993).
- ¹² M. C. Collins, "A self-starter for the parabolic equation method," *J. Acoust. Soc. Am.* **92**, 2069–2074 (1992).
- ¹³ N. C. Makris, J. M. Berkson, T. L. Krout, and R. Menis, Environmental/Navigation, Sections 7.1–7.4, in "Acoustic Reverberation Special Research Program Acoustic Reconnaissance Experiment, Initial Report," Scripps Institution of Oceanography (1991).
- ¹⁴ B. E. Tucholke, M. C. Kleinrock, and W. K. Stewart, "Geological and Geophysical Characteristics of the Acoustic Reverberation Corridor, and their Relevance to the Conduct of G&G Fine-Scale Surveys," *Acoustic Reverberation Special Research Program Research Symposium*, Scripps Institution of Oceanography (1993).
- ¹⁵ B. D. Steinberg, *Principles of Aperture and Array System Design* (Wiley, New York, 1976).
- ¹⁶ A paper on mapping, inverting, and projecting high-resolution reverberation data onto bathymetry is in preparation for submission to *J. Acoust. Soc. Am.*
- ¹⁷ N. C. Makris, J. M. Berkson, R. Menis, and G. L. Gibian, "Mapping Direct Path ARC Backscatter onto High Resolution Bathymetry," *Acoustic Reverberation Special Research Program Research Symposium*, Scripps Institution of Oceanography (1993).
- ¹⁸ B. E. Tucholke and J. Lin, "Detachment Faulting and Its Relation to Geologic Structure at First- and Second-Order Offsets of Slow-Spreading Ridges," *EOS* **73**, 286 (1992).
- ¹⁹ B. E. Tucholke, J. Lin, and M. C. Kleinrock, "Crustal Structure of Spreading Segments on the Western Flank of the Mid-Atlantic Ridge at 25° 25' to 27° 10' N," *EOS* **73**, 537–538 (1993).
- ²⁰ N. C. Makris, J. M. Berkson, R. Menis, and L. Alvelino, Preliminary

- Results: Correlation between Reverberation and Geomorphology, in "Acoustic Reverberation Special Research Program Main Acoustic Experiment, Initial Report," Scripps Institution of Oceanography (1993).
- ²¹P. M. Ogden and F. T. Erskine, "Low-frequency Surface and Bottom Scattering Strengths Measured Using SUS Charges," in *Ocean Reverberation*, edited by D. Ellis, J. Preston, and H. Urban (Kluwer, Dordrecht, 1993).
- ²²N. C. Makris, J. M. Berkson, and R. Menis, "High Resolution Backscatter from the Mid-Atlantic Ridge," *J. Acoust. Soc. Am.* **94**, 1802 (1993).
- ²³A paper on the results of the Main Acoustics Exp. of 1993 is in preparation for submission to *J. Acoust. Soc. Am.*
- ²⁴I. Dyer, A. B. Baggeroer, J. D. Zittel, and R. J. Williams, "Acoustic Backscattering from the Basin and Margins of the Arctic Ocean," *J. Geophys. Res.* **87**, 9477-9488 (1982).